

Data driven foreground clustering approach to component separation in multifrequency CMB experiments: A new Planck CMB map

Rishi Khatri^a

^aDepartment of Theoretical Physics, Tata Institute of Fundamental Research, Homi Bhabha Road, Mumbai 400005, India

E-mail: khatri@theory.tifr.res.in

Abstract. We present a new approach to component separation in multifrequency CMB experiments by formulating the problem as that of partitioning the sky into pixel clusters such that within each pixel cluster the foregrounds have similar spectrum, using only the information available in the data. Only spectral information is used for partitioning, allowing spatially far away pixels to belong to the same cluster if their foreground properties are close. We then apply a modified internal linear combination method to each pixel cluster. Since the foregrounds have similar spectrum within each cluster, the number of components required to describe the foregrounds is smaller compared to all data taken together and simple pixel based ILC algorithm works extremely well. We test our algorithm in the full focal plane simulations provided by the Planck collaboration. We apply our algorithm to the Planck full mission data and compare our CMB maps with the CMB maps released by the Planck collaboration. We show that our CMB maps are clean and unbiased on a larger fraction of the sky, especially at the low Galactic latitudes, compared to publicly available maps released by the Planck collaboration. This is important for constraining beyond the simplest Λ CDM cosmological models and study of anomalies. Our cleaned CMB maps are made publicly available for use by the cosmology community.

Keywords: cosmic background radiation, cosmology:theory, early universe

Contents

1	Introduction	1
2	Data driven foreground clustering (FC)	3
2.1	Choosing the number of pixel clusters (partitions)	4
2.2	Choosing the partition boundaries	4
3	Internal linear combination: FC-ILC	7
3.1	Combining information from maps with different resolutions	9
3.2	Masks	11
3.3	Results for FFP6 simulations	12
4	A new foreground cleaned Planck CMB map	12
4.1	Angular power spectrum at $2 \leq \ell \leq 29$	12
4.2	Angular power spectrum for $30 \leq \ell \leq 800$	13
4.3	Angular power spectrum at $800 \leq \ell \leq 2500$	14
5	Conclusions and remarks about possible improvements	16
A	Convergence of FC-ILC solution	20

1 Introduction

The Cosmic Microwave Background (CMB) experiments observe the sky in broad frequency bands. The data thus obtained contains not only the CMB but emission from gas and dust in our own Galaxy as well as the integrated emission from all the galaxies since the formation of the first stars. There is a broad window where the CMB dominates over all other astrophysical emissions in a large part of the sky and the CMB experiments from the ground as well as space have taken advantage of this. With the Planck experiment [1] and the ground based experiments such as South Pole Telescope (SPT) [2], Atacama Cosmology Telescope (ACT) [3] and BICEP2 [4], the experimental sensitivity has reached a point where we are limited not by the detector noise but by the residual foreground contamination in the data. Multifrequency experiments such as Wilkinson Microwave Anisotropy Probe (WMAP) [5] and Planck allow us to use the fact that the CMB and the foregrounds have different frequency spectrum to separate the CMB from the other Galactic and extragalactic components present in the data. However, in any experiment, we have a limited number of channels available while the foreground properties, the amplitude as well as the shape of the spectrum of different physical components, such as thermal and spinning dust emission, line emission from CO and other molecules and atoms, synchrotron emission etc., vary over the sky from pixel to pixel.

If we have a physical parametric model for all the cosmological components and the foregrounds, and a sufficient number of frequency channels, we can fit for the parameters of the model in each pixel. This is the approach followed in the Commander [6] and Linearized Iterative Least-squares (LIL) [7] algorithms. However, the measured intensity in every frequency band in any given

pixel is a superposition of many different sources along the line of sight. For example, thermal dust emission from many molecular clouds along the line of sight, which may have different physical properties such as temperature, and different angular sizes on the sky, may contribute to the intensity observed in a single pixel. This makes the description of the foreground emissions by simple parametric models, at the required accuracy, difficult. These difficulties have been the motivation towards the development of the so called non-parametric or *blind* component separation methods which need only the spectrum of the cosmological signal of interest to be known. These methods, in particular, do not need any knowledge about the foregrounds except that their spectrum is different from the signal of interest and some additional statistical requirements about the independence of components or that the angular variations of the foregrounds are uncorrelated with the signal of interest. These methods such as Spectral Estimation Via Expectation Maximization (SEVEM) [8], Spectral Matching Independent Component Analysis (SMICA) [9, 10], Fast Independent Component Analysis (FASTICA) [11], Needlet Internal Linear Combination (NILC) [12], scale discretized ILC (SILC) [13] or iterative ILC approach [14] compute the desired cosmological signal (e.g. CMB) map as a linear combination of the available different frequency channel sky maps. Different choices of how we combine the available frequency channel maps and what quantity we optimize to get the weights at different frequencies gives us different algorithms. These blind algorithms however work best when the foregrounds can be described by the superposition of a small number of spectral shapes, smaller than the number of frequency channels available. As we noticed earlier, the foreground properties, specifically the spectral shape of the foregrounds, varies over the sky. This means that we cannot apply a blind algorithm to the full sky but must divide the data into clusters such that within each cluster the data can be described by a superposition of a small number of foreground components. Different criteria for clustering of the data will lead to different solutions for the cosmological signal. The above mentioned algorithms differ also in how they cluster or partition the data, with SEVEM clustering the data in pixel space into a small number of regions based on the *amplitude* of the foregrounds, SMICA clusters the data in harmonic space with the weights a function of the multipole ℓ and NILC clusters the data using spherical needlets achieving localization or clustering in broad multipole bands as well as in real space. In all of these cases, the clustering or partitioning of the data is done without using the information about the foreground spectrum available in the data but is instead motivated more by heuristic arguments and prior assumptions about the foregrounds. Also, all current algorithms use a single partitioning of data with some smoothing prescription across the partitions. It is not clear a priori why a particular partitioning scheme should be chosen over another and whether there exists a single optimal partitioning of the data given our limited knowledge of foregrounds and limited number of frequency channels available.

The main new feature of our approach that distinguishes it from the existing algorithms is how we cluster the data. We will work in pixel space and use Internal Linear Combination (ILC) [15–18] as our component separation method within each cluster. However the basic ideas about the partitioning of data can be applied in any other basis, including the spherical harmonic basis, and any other basic component separation algorithm. The following two main ideas underlie our new approach to component separation:

1. There is no single optimal partitioning of the data, given our limited knowledge of the foregrounds. We must therefore explore all possible partitionings probabilistically, subject to the

constraint in the second point. We will see that this approach automatically blurs the boundaries between the partition and thus does not require any extra smoothing across the partition boundaries. By allowing the partitions or clustering of the data to vary we essentially want to take into account the uncertainties in our knowledge of the foregrounds.

2. The data should be clustered so that the data within each cluster has similar foreground properties, in particular the spectrum, since we will be using the spectral information to distinguish the signal of interest from other components.

We note that such a problem on *clustering* of data is well suited for machine learning and in that context it also goes by the name of *unsupervised learning*. We will however not go by the machine learning route but follow a very simple prescription for the clustering of data with the spectral properties of the foregrounds quantified by a single parameter i.e. we will cluster data along a single dimension. We will see that our simple approach already works very well for Planck data and motivates more sophisticated machine learning based clustering in more than one dimensions as well as Bayesian extensions [19] which we leave for future work. In particular, the small number of high resolution frequency channels available in Planck do not allow a more sophisticated clustering approach than a single parameter one we describe below. A single parameter is however not sufficient to quantify the differences in shapes of multicomponent foregrounds. Future experiments such as LiteBIRD [20], Primordial Inflation Explorer (PIXIE) [21], Cosmic Origins Explorer (CORE) [22] and Probe of Inflation and Cosmic Origins (PICO) [23] would have more than twice the number of channels available in Planck and would allow implementation of more accurate multi-parameter clustering as well as use of machine learning to partition the data.

In this paper we will be only interested in the CMB to demonstrate our algorithm but it can equally well be used for any other component for which the spectrum is known, such as the Sunyaev-Zeldovich (SZ) effect [24]. We will explore the SZ effect and other applications in separate publications. We make the full sky cleaned CMB maps constructed from the Planck public release 2 (PR2) data release [25] by our algorithm publicly available.

2 Data driven foreground clustering (FC)

We want to construct a measure which can tell us how close or far apart two pixels are in terms of their foreground properties other than the amplitude. We will be using Planck data from 70 GHz to 545 GHz, where the main foreground for the CMB is dust emission. We construct a very simple measure by subtracting the 100 GHz map from the 545 GHz and 353 GHz maps and then take the ratio of the resulting maps to get the measure $m(p)$ at each pixel p ,

$$m(p) = \frac{T_{545\text{GHz}}(p) - T_{100\text{GHz}}(p)}{T_{353\text{GHz}}(p) - T_{100\text{GHz}}(p)}, \quad (2.1)$$

where T_ν is the map at frequency ν in units of K_{CMB} . The choice of measure is dictated by the fact that we need two foreground dominated channels from which we want to subtract out the CMB, estimated from a channel which is not only relatively cleaner but also does not have too much noise. We note that this measure will capture how fast the total foreground emission is increasing or decreasing with frequency and therefore would capture information about the dust emission or strong synchrotron

sources. However, such a measure would miss components like CO emission which are present in some channels but not others. Using this measure also limits us to use the channels which do not have significant synchrotron emission since it is not captured by our measure. In particular we will not be using 30 GHz and 44 GHz channels for this reason. In principle it is possible to construct a second measure which would capture the synchrotron emission, it will however complicate the clustering. In this early stage of exploring a new approach to component separation, we want to keep things as simple as possible and leave further sophistication to future work. Due to these reasons we do not expect the clustering to be optimal. By optimal clustering we mean the clustering where foregrounds in each cluster can be described by a number of components smaller than the number of frequency channels available. We will see that such a simple measure works reasonably well for Planck in particular because CO emission is not a big contaminant for the CMB. Our results will motivate exploring more sophisticated clustering for Planck as well as future experiments with higher sensitivity and more frequency channels taking into account the line emissions in each pixel in addition to the continuum emission.

To suppress fluctuations in the measure due to the noise, especially from the 100 GHz channel, and make sure that we are dominated by signal in every pixel, we first smooth all maps to $15'$ before calculating the measure. In particular we want to suppress noise in the difference maps in the low foreground pixels at high latitudes. We show the probability density function (PDF) of the measure, $P(m)$, at $15'$ resolution, for the Planck FFP6 (Full Focal Plane) simulations [26] as well as the PR2 data in Fig. 1. A majority of the pixels are at $7 \lesssim m \lesssim 25$ but there is a large tail at $m > 25$ and a smaller tail at $m < 0$. The $m > 25$ tail is coming from the infrared point sources while the negative m tail is coming from the low frequency radio sources for which 353 GHz temperature is smaller than the 100 GHz temperature. The measure m therefore naturally separates out the strongest point sources and we put all pixels with $m < 7$ or $m > 25$ into one bad cluster. We then extend this *bad region* or mask by $5'$. These pixels should be masked in any cosmological analysis. There are two choices we must now make: How many clusters we should partition the data into and where should we place the partition boundaries.

2.1 Choosing the number of pixel clusters (partitions)

We want to partition the rest of the pixels between our cutoffs, $7 \leq m \leq 25$, into smaller clusters and apply the ILC algorithm to each cluster. The number of clusters should not be too large, since then the ILC bias in each cluster could be large when we have only a small amount of data in each cluster. The number of clusters should not be too small since then the foregrounds in each cluster would be too complicated. We choose to have 12 clusters + 1 bad cluster of point sources giving a total of 13 clusters of pixels. Our algorithm is not very sensitive to the exact number of clusters and we get very similar results if, for example, instead of 13 clusters we have 23 or 7 clusters. We show the effect of choosing different number of clusters or partitions in Appendix A.

2.2 Choosing the partition boundaries

We want to cluster the pixels so that the pixels closer together in m value are in the same cluster. The simplest way would be to divide the m range spanned by the data into equal intervals. This will however lead to a problem of too few pixels in the clusters away from the main peak of the PDF with most of the pixels in a single cluster. We instead sort the pixels according to their m value. We

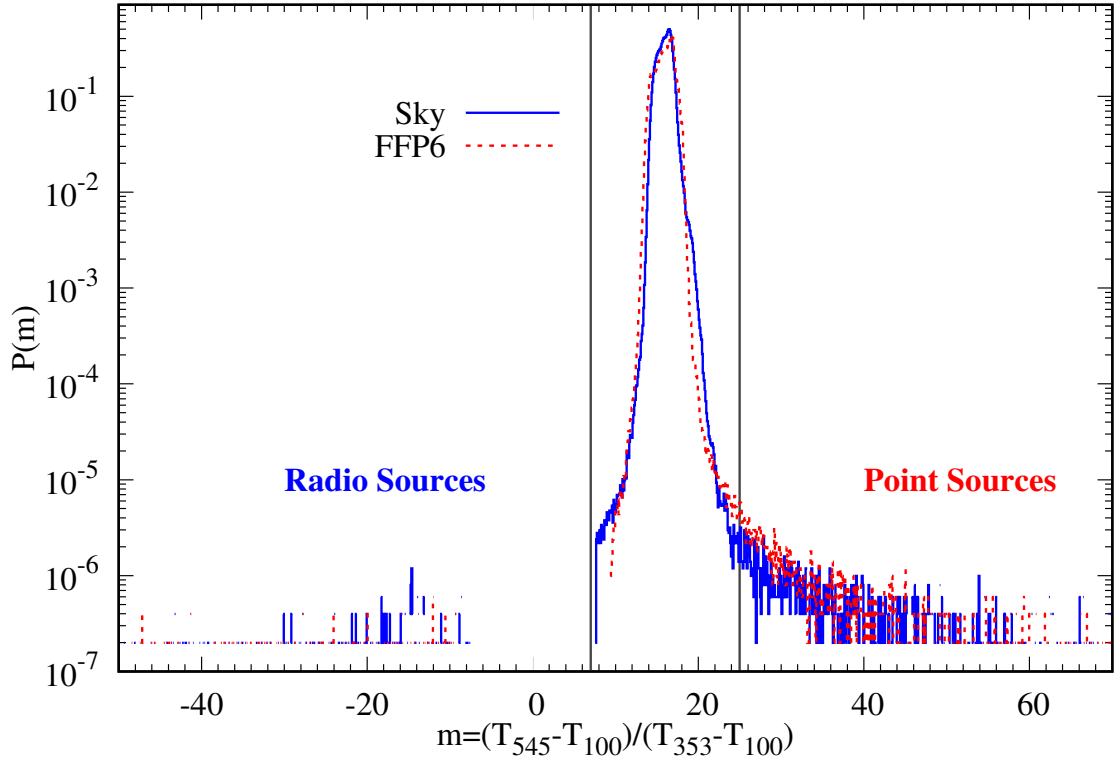


Figure 1: PDF of the measure m for the FFP6 simulations and Planck PR2 sky. The two tails of the PDF correspond to the point sources in radio and far infrared. The two vertical lines show the cutoffs we put to remove strong point sources which are put in a separate *bad cluster*, cluster number 0 below.

can now partition the sorted pixel array so that each cluster has equal number of pixels. However any fixed clustering seems a bit arbitrary, since the pixels at the boundary would be closer in their m value to the pixels just across the cluster boundary than the pixels in the same cluster near the other boundary of the cluster.

What we would like is that the ILC solution at each pixel is influenced most by the pixels nearest to it in m value and less and less as we move away in m . Equivalently the pixels closest to a given pixel in the m -sorted pixel array should most strongly influence it and the pixels further and further away in the array have lesser and lesser influence in deciding the ILC solution or weights. We therefore choose the following algorithm for the clustering:

1. Randomly choose partitions uniformly between the minimum pixel position in the sorted array p_{\min} and the maximum p_{\max} , the minimum and maximum corresponding to the cutoffs we placed at the tails of the PDF $P(m)$.
2. Perform ILC in each cluster.
3. Repeat the above steps N times, each time with a new random realization of partitions.
4. The final solution at each pixel is obtained by average of the N solutions.

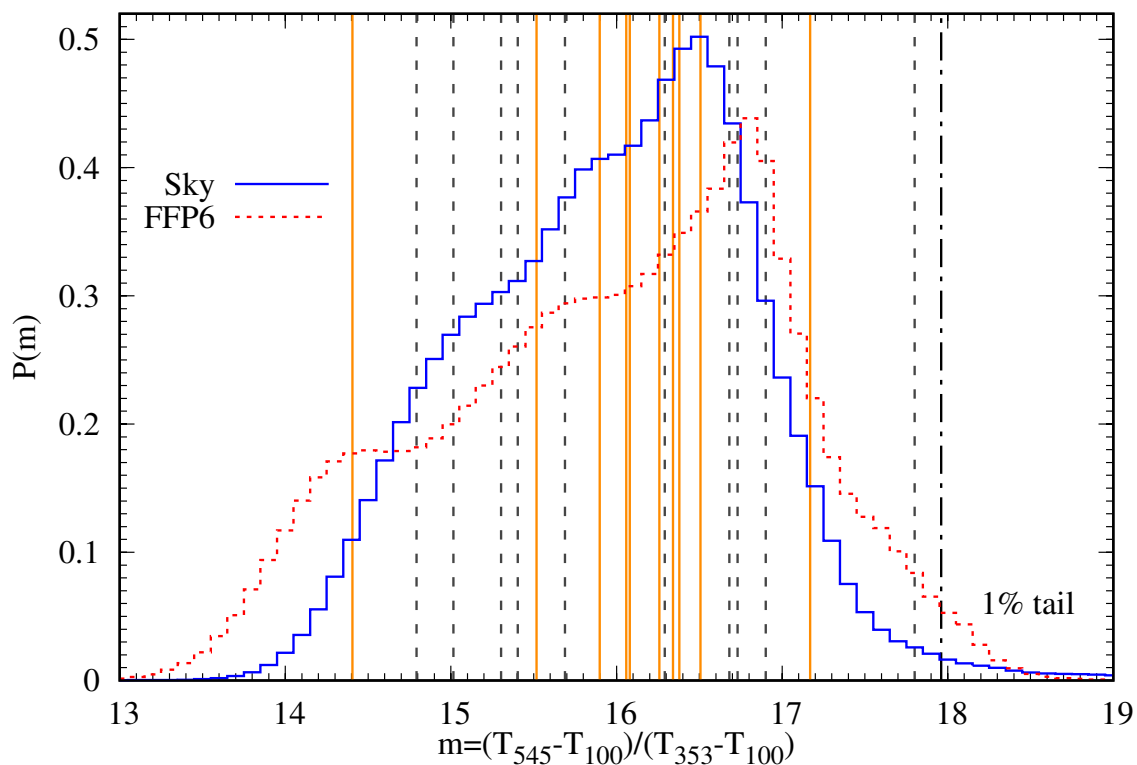


Figure 2: PDF of the measure m for the FFP6 simulations and Planck PR2 sky. We show two random realizations of partitions by vertical solid and dashed lines. The rightmost partition (dot-dashed curve) is a fixed partition containing the 1% of the most contaminated pixels.

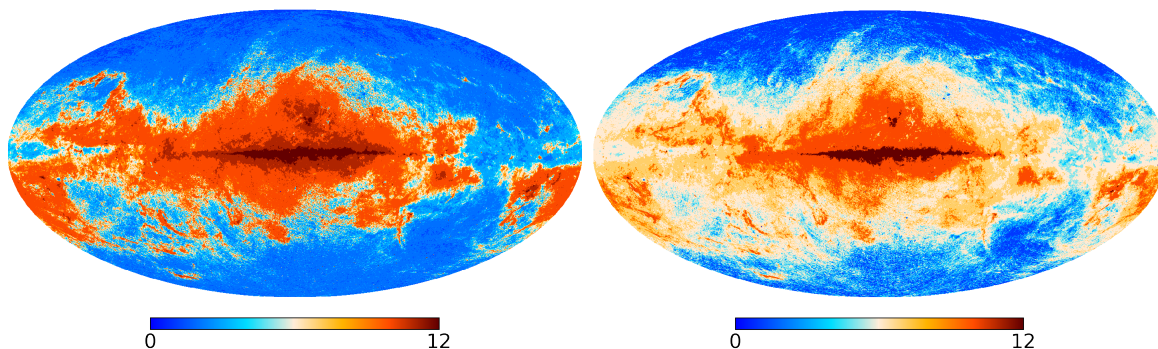


Figure 3: Two random realizations of clustering for Planck PR2 sky. Each pixel value, between 0 and 12, corresponds to the cluster number it belongs to.

We show two such random partitionings in Fig. 2. We see that the some partitions are quite small while others are large. The advantage of the above procedure is that there is automatically a larger probability that pixels closer to each other would find themselves in the same cluster more often compared to pixels further away which is what we want. Also, the partition boundaries are automatically blurred as they are randomly chosen each time and there is no need for any other

smoothing. We find that the solution converges very rapidly as we increase N and after $N = 100$ there is no noticeable change in the final solution. The convergence with the increasing N is shown and further discussed in Appendix A. In particular the change in FC-ILC solution when doubling N from 100 to 200 is < 1 μK at $N_{\text{side}} = 512$ resolution, except for a few extremely contaminated pixels in the two bad clusters, indicating that the algorithm has converged to a desired level. We therefore choose this value of N . The high values of m also correspond to the most contaminated regions on the sky near the Galactic center which also have more complicated foreground properties. We do not want these regions to influence the ILC solution in the neighbouring regions. We therefore put the pixels belonging to the 1% high m tail of $P(m)$ in a fixed cluster (see Fig. 2) and choose random partition boundaries for only the remaining 11 pixel clusters. The maps of two random realizations of clustering are shown in Fig. 3.

3 Internal linear combination: FC-ILC

We want to separate out the cosmological signal of interest, in this paper the CMB, from other cosmological components and galactic foregrounds in each pixel cluster or partition. We note that similar to the usual ILC, our method can also be used to look for any other signal with known spectrum, the generalization usually going by the name of Generalized ILC in CMB literature. The generalization is quite trivial and just involves transforming the data into units in which the desired signal is the same in all frequency channels and then applying the ILC method described below.

The observed data, $T_i(p)$ in each pixel p in frequency channel i can be written, in K_{CMB} units as

$$T_i(p) = s_{\text{CMB}}(p) + f_i(p) + n_i(p), \quad (3.1)$$

where s_{CMB} is the CMB temperature independent of frequency but a function of pixel number p , f_i is sum of all other components which have a different spectrum than the CMB and are therefore a function of the frequency channel i as well as the pixel number p and $n_i(p)$ is the noise in channel i and pixel p . We will be using HEALPix (Hierarchical Equal Area Iso Latitude pixelation of the sphere [27]) pixelization and p denotes the pixel number in one of the HEALPix ordering schemes. We want to construct a linear combination of data T_i which preserves the desired signal, s_{CMB} , i.e. we want to find weights, w_i^α for each pixel cluster α such that,

$$\hat{s}_{\text{CMB}}(p^\alpha) = \sum_i w_i^\alpha T_i(p^\alpha) \quad (3.2)$$

$$\sum_i w_i^\alpha = 1, \quad (3.3)$$

where p^α is the pixel belonging to partition α , and \hat{s}_{CMB} is our solution for the CMB signal,

$$\hat{s}_{\text{CMB}}(p^\alpha) = s_{\text{CMB}}(p^\alpha) + \sum_i w_i^\alpha [f_i(p^\alpha) + n_i(p^\alpha)]. \quad (3.4)$$

We want to choose w_i^α such that the foregrounds and noise contribution to \hat{s}_{CMB} , the second term in the above equation, is minimized. Put another way, we want \hat{s}_{CMB} to be as close to s_{CMB} as possible.

This suggests the following cost function to be minimized,

$$\begin{aligned}
C' &= \sum_{p^\alpha} [\hat{s}_{\text{CMB}}(p^\alpha) - s_{\text{CMB}}(p^\alpha)]^2 \\
&= \sum_{p^\alpha} \left[\sum_i w_i^\alpha (f_i(p^\alpha) + n_i(p^\alpha)) \right]^2.
\end{aligned} \tag{3.5}$$

Clearly, when the weights are chosen so that C' is minimized the residuals from the combination of foregrounds and noise in our estimator \hat{s}_{CMB} are minimum. However, we cannot compute the cost function C' from the data since it depends upon the true signal s_{CMB} . We have access to only \hat{s}_{CMB} . We can therefore try to minimize the following cost function, which can be computed from the data, as the next best thing,

$$\begin{aligned}
C &= \sum_{p^\alpha} [\hat{s}_{\text{CMB}}(p^\alpha)]^2 \\
&= \sum_{p^\alpha} s_{\text{CMB}}(p^\alpha)^2 + C' + 2 \sum_{p^\alpha} s_{\text{CMB}}(p^\alpha) \sum_i w_i^\alpha [f_i(p^\alpha) + n_i(p^\alpha)].
\end{aligned} \tag{3.6}$$

Since the first term does not depend on w_i^α , minimizing C will be equivalent to minimizing C' if the last term vanishes, i.e. the signal is uncorrelated with the foregrounds. We note that the instrumental noise in most experiments would be uncorrelated with the signal and the foregrounds but there maybe some chance correlation between the foregrounds and the signal given the finite amount of data, especially on large scales where the number of independent modes is very small. This chance correlation means that the last term in Eq. 3.6 is not zero and minimizing C is not equivalent to minimizing C' . We will therefore get a biased result, with the ILC solution also removing the part of the signal correlated with the foregrounds. This is known as the ILC bias [12, 15, 28] and is the price we pay for not knowing a priori the spectrum of the foregrounds in such blind algorithms. The ILC bias results in a solution which has less power than the actual signal. We find that in FFP6 simulations the ILC bias is significant, with our algorithm, only for the quadrupole ($\ell = 2$) and is negligible for all higher multipoles. However, it can start affecting higher multipoles if we increase the number of partitions to a very high number.

We note that our cost function C is not the covariance matrix that is usually used in the ILC. The covariance matrix usually minimized in standard ILC is defined by

$$\text{Cov} = \sum_{p^\alpha} [\hat{s}_{\text{CMB}}(p^\alpha) - \langle \hat{s}_{\text{CMB}}(p^\alpha) \rangle]^2, \tag{3.7}$$

where $\langle \hat{s}_{\text{CMB}}(p^\alpha) \rangle$ is the average value of \hat{s}_{CMB} of the pixels in the partition α . In general C and Cov would have different foreground properties and will give different results. Which of the two is better would depend on the signal as well as the nature of data. For Planck data, we find that using C as the cost function to be optimized gives slightly better results for the CMB both in the FFP6 simulations as well as on the real sky. Since in Planck data, with the zero level set to the Galactic zero levels, the CMB already has a zero mean while most of the foregrounds are strictly positive, we can expect that trying to remove all foregrounds, including the average foreground signal, in a cluster would give better results. Another possibility is that the Covariance matrix has slightly more complicated foregrounds properties resulting in a slightly worse solution. Also, minimizing the Cov would leave

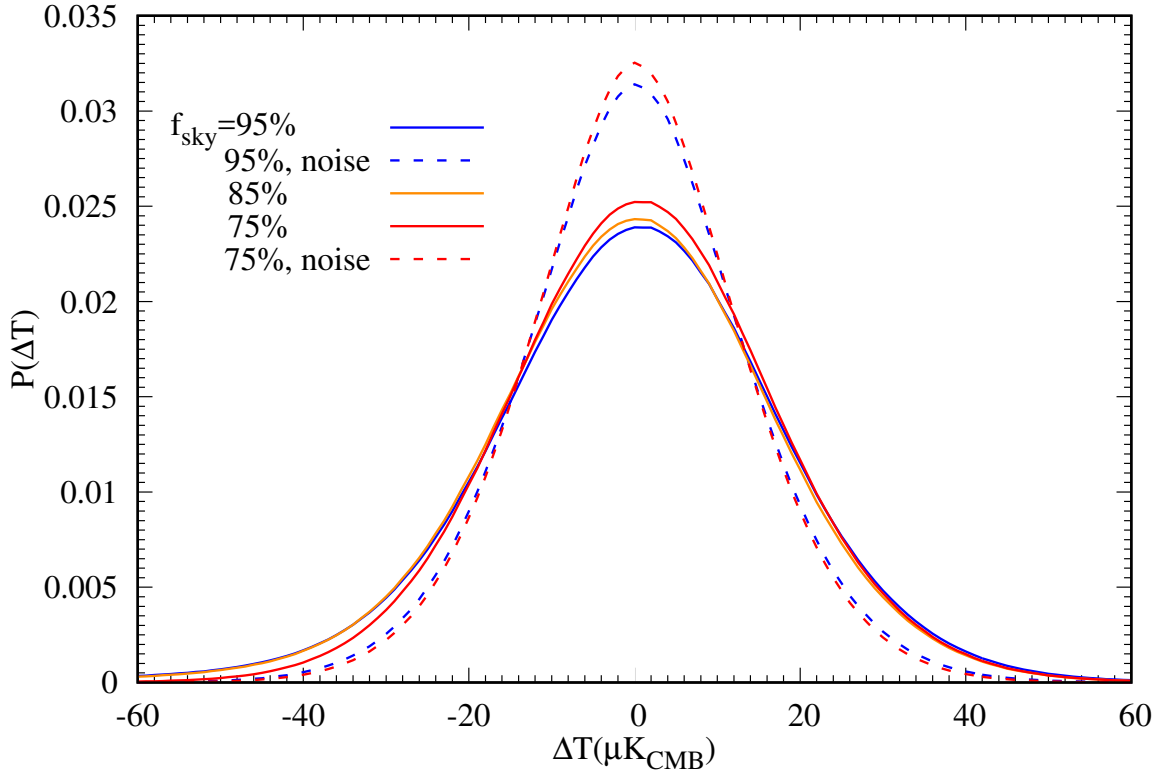


Figure 4: The probability density function of the difference between the input CMB map and the ILC solution, after removing the monopole, the dipole, and the quadrupole at full resolution $N_{\text{side}} = 2048$. The red and blue dashed lines are the noise PDF from half ring half difference maps for 75% and 95% sky fractions respectively at the map resolution of $5'$. For most pixels, the difference is consistent with the noise, the small foreground contamination shows up in the tails of the PDF.

a residual average bias in each cluster, since we are subtracting the average signal from the partial sky, which may bias the large scale modes. We therefore use C in Eq. 3.6 as our cost function to be optimized.

We now define the matrix \mathbf{D} as

$$\mathbf{D}^{\alpha}_{ij} \equiv \sum_{p^{\alpha}} T_i(p^{\alpha}) T_j(p^{\alpha}). \quad (3.8)$$

The usual minimization using Lagrange multipliers [18] gives the ILC solution in each partition,

$$w_i^{\alpha} = \frac{\sum_j \mathbf{D}^{\alpha-1}_{ij}}{\sum_{ij} \mathbf{D}^{\alpha-1}_{ij}}. \quad (3.9)$$

As explained earlier, we choose partitions randomly and get the ILC solution in each pixel $N = 100$ times and the final solution is the average of N solutions.

3.1 Combining information from maps with different resolutions

Before we apply our algorithm, we must also find a way to optimally combine the information from maps at different frequencies which in any CMB experiment usually have different resolutions. This

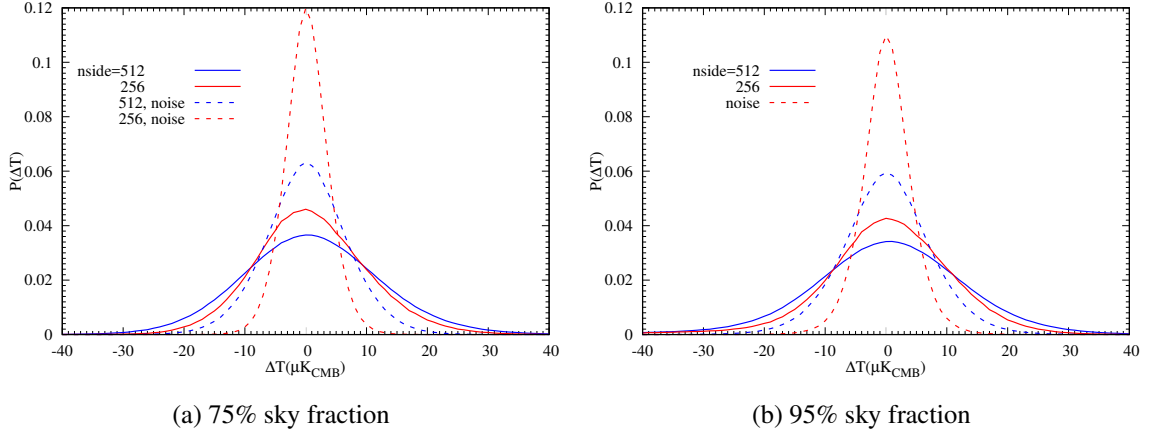


Figure 5: The probability density function of the difference between the input CMB map and the ILC solution, after removing the monopole, the dipole, and the quadrupole at resolutions $N_{\text{side}} = 512, 256$. The red and blue dashed lines are the noise PDF from half ring half difference maps. For most pixels, the difference is consistent with the noise, the small foreground contamination shows up in the tails of the PDF. The suppression of noise at lower resolution means that more pixels are dominated by contamination as we decrease the resolution as evident by the growing difference between the noise and CMB pdfs. We note that the average size of a pixel at $N_{\text{side}} = 512$ resolution is 6.87 arcmin, close to the resolution of the map and is therefore a fair representation of the contamination in the map.

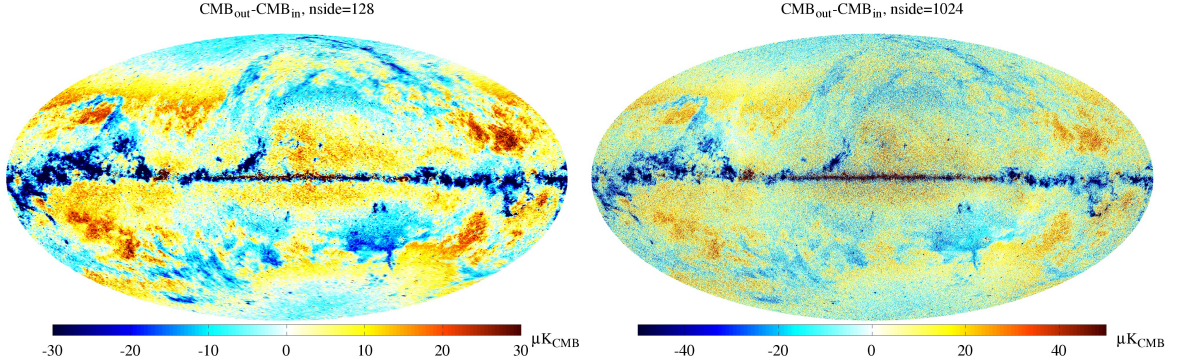


Figure 6: The difference between the input map and FC-ILC solution for the FFP6 simulation at HEALPix resolution $N_{\text{side}} = 128$ and $N_{\text{side}} = 1024$. For most of the sky the difference is less than $10\mu\text{K}$ for $N_{\text{side}} = 128$.

poses a conundrum for the pixel space component separation algorithms. Noise in a frequency channel affects the weight it gets. However, noise per pixel depends on the resolution of the map. We should therefore first rebeam all maps to a common resolution. If we rebeam all maps to a common resolution corresponding to the lowest resolution map, we loose small scale information. If we rebeam all maps to highest resolution maps, the noise in lower resolution maps would be boosted and the ILC solution will down weight these maps heavily, effectively loosing any information contained in these maps. In the harmonic space methods this is not a problem since after all maps have been rebeamed to the highest resolution, the noise in each map would shoot only on scales smaller than the

Min Freq - Max Freq	Number of channels	Resolution (Gaussian Beam FWHM)
70 GHz - 545 GHz	6	15'
100 GHz - 545 GHz	5	10'
143 GHz - 545 GHz	4	7.5'
217 GHz - 545 GHz	3	5'

Table 1: Planck frequency channel combinations and the rebeaming resolution used for FC-ILC solutions presented in this paper. All maps are rebeamed to have Gaussian beams.

beam size or at high ℓ . Therefore, for each ℓ mode, all channels with sufficient signal to noise ratio provide information and contribute to the ILC solution. We want the same advantage but in pixel space. To achieve this, we have come up with the following algorithm.

1. Rebeam all maps to lowest resolution map and apply FC-ILC algorithm. This solution will have the lowest foregrounds at that resolution since it uses the information from the maximum number of channels. Let's label the ILC solutions by index a , i.e. \hat{s}_{CMB}^a , with $a = 1$ corresponding to the lowest resolution, and $a > b$ implying resolution of map a is higher than map b . We will denote the corresponding (Gaussian) beams with b_ℓ^a .
2. Now drop the lowest resolution channel, rebeam all maps to the next higher resolution and obtain a new ILC solution.
3. Repeat step 2 until not enough frequency channels remain to get a viable ILC solution
4. Combine the n solutions at different resolutions \hat{s}_{CMB}^a in harmonic space, i.e. $a_{\ell m}^a$, to get the final solution \hat{s}_{CMB}^f , or in harmonic space $a_{\ell m}^f$, with the resolution corresponding to the highest resolution channel with beam b_ℓ^n , as follows:

$$a_{\ell m}^f = b_\ell^n \left[a_{\ell m}^1 + (1 - b_\ell^1) \left(a_{\ell m}^2 + (1 - b_\ell^2) \left(a_{\ell m}^3 + \dots + (1 - b_\ell^{n-1}) \frac{a_{\ell m}^n}{b_\ell^n} \right) \right) \right]. \quad (3.10)$$

In the last term in nested brackets in the above equation, we correct the highest resolution solution with its beam and then use the resulting $a_{\ell m}$ to fill in only the information not present in the next lower resolution map, hence the factor of $(1 - b_\ell^{n-1})$. We then use the result to fill in only the information not present in the next lower resolution map and so on until the lowest resolution map. The final result is multiplied by b_ℓ^n to get the final map at the highest resolution possible. Note that b_ℓ^a are the beam functions of the rebeamed maps and we use Gaussian beams for rebeaming. The beams used for different Planck channel combinations are given in Table 1.

3.2 Masks

We create masks with different sky fractions by first masking pixels above a certain threshold in m map to remove few % of highest m pixels, which also masks most of the point sources and then extend this mask by removing the pixels above a threshold in the 545GHz map after smoothing it

with a Gaussian beam of $90'$ FWHM. All masks for calculating the power spectrum are apodized by a Gaussian replacing 1s in the mask by $1 - \exp(-9\theta^2/(2\theta_{\text{ap}}^2))$ for $\theta < \theta_{\text{ap}} = 30'$, the apodization angle, where θ is the distance of the pixel from the nearest masked (0 value) pixel.

3.3 Results for FFP6 simulations

The result of applying our FC-ILC algorithm on the Planck FFP6 simulations is shown in Fig. 4 where we show the probability density function (PDF) of the difference between the input map and the FC-ILC map at full resolution for different sky fractions after removing the monopole, dipole and also the quadrupole since we expect to have a small bias in the quadrupole. For most of the pixels, the difference is dominated by noise. In a small fraction of pixels the foreground residuals result in a thicker tail compared to the Gaussian noise. The noise PDF is calculated from the half-ring half-difference maps. We show in Fig. 5 the PDFs for lower resolutions of $N_{\text{side}} = 512$ and 256. At lower resolutions the noise is suppressed increasing the width of the CMB pdfs compared to the noise pdfs. The resolution of $N_{\text{side}} = 512$ has an average pixel size of 6.87 arcmin, close to the resolution of our maps and is therefore a fair representation of the noise and contamination in our maps.

We show in Fig. 6 the difference maps at HEALPix $N_{\text{side}} = 128$ and 1024 and in Fig. 7 the angular power spectrum C_ℓ as a function of the multipole ℓ . There is significant ILC bias only for the quadrupole. At $\ell \gtrsim 1500$ the excess is due to the residual foregrounds. We have plotted the SMICA C_ℓ also for the similar sky fraction from Fig. E.4 in [29]. We see that $\ell \gtrsim 2000$ FC-ILC slightly outperforms SMICA but performs as well as NILC. However, we should keep in mind that our masks, even though they cover a similar sky fraction, are different from those used in [29] and could be the cause of the slightly larger excess in the SMICA curve. We note that SMICA has the smallest contamination among all algorithms in Fig. 10 in [29] when applied to real data.

We conclude that our algorithm FC-ILC, on the FFP6 simulations, performs at least as well as the existing algorithms, perhaps even slightly better.

4 A new foreground cleaned Planck CMB map

We have applied our algorithm to the Planck PR2 release maps. The CMB map at $5'$ resolution is shown in Fig. 8. We calculate the angular power spectrum as a cross spectrum between the half-ring maps using the PolSpice software [30, 31] get the *pseudo* C_ℓ which have been deconvolved from the effects of the masks and corrected for the beam. PolSpice also calculates the analytical covariance matrix [see also 32, 33] which we use to estimate the error bars. We then bin the angular power spectrum $D_\ell \equiv \ell(\ell + 1)C_\ell/(2\pi)$ as well as the covariance matrix in ℓ bins which increase in width with ℓ for $\ell \geq 30$.

4.1 Angular power spectrum at $2 \leq \ell \leq 29$

We show the power spectrum for $2 \leq \ell \leq 29$ for a sky fraction of 95% in Fig. 9. Also shown is the best estimate of the power spectrum in the PR2 release of Planck collaboration [1] by solid line and the power spectra estimated from the SMICA, NILC, Commander, and SEVEM maps released by the Planck collaboration [34] and calculated with the same mask. We note that the power spectra estimated from the cleaned CMB maps are the pseudo C_ℓ s and would therefore show some oscillations because of the de-convolution of the mask. However, we expect these systematics due to the

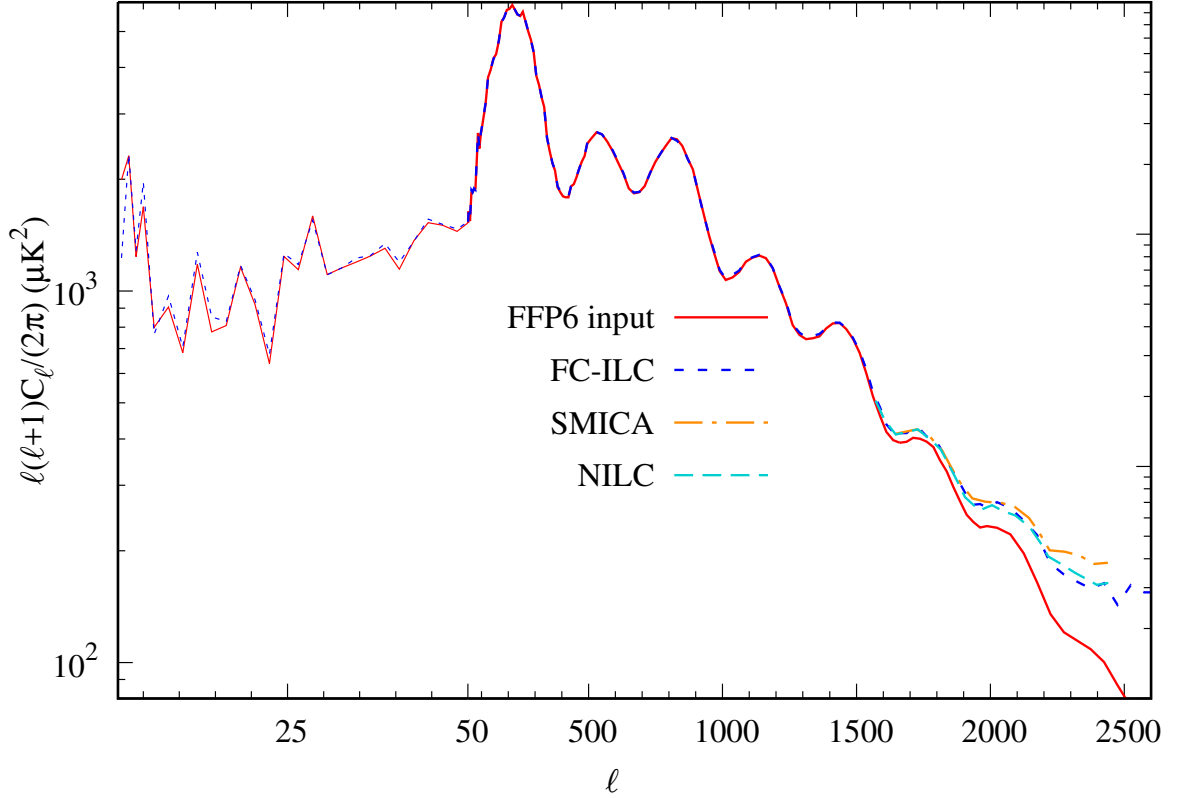


Figure 7: The FC-ILC angular power spectrum for 72% sky fraction compared with the power spectrum of the input map with same mask calculated using PolSpice software [30, 31] which analytically deconvolves the mask in real space (equivalent to the harmonic space deconvolution by XSPECT [32, 33]). We also show the SMICA and NILC solutions for FFP6 for large ℓ modes taken from [29]. There is ILC bias for quadrupole, which is expected, but it is negligible for all higher multipoles. For highest multipoles our algorithm has slightly smaller residual foregrounds compared to the similar sky fraction for SMICA.

incomplete sky to be not significant since we are use a very large fraction of the sky. All maps seem to be in rough agreement with the released power spectrum. FC-ILC shows a slightly larger deviation compared to the other maps. However, this deviation is for the ℓ values for which the power spectrum deviates considerably for all of the maps shown. We note that the ILC bias at $\ell = 2$ is less compared to what we saw in the FFP6 simulations. This may mean that either the best estimate of the quadrupole in Planck 2015 release is biased and therefore closer to the ILC solution or that the foregrounds have smaller correlation with the CMB in the real sky compared to the simulations. Given the consistency of Planck with WMAP [5], the latter is most likely the correct explanation.

4.2 Angular power spectrum for $30 \leq \ell \leq 800$

We show the binned angular power spectrum for $30 \leq \ell \leq 800$ in Figs. 10 and 11 for the sky fraction of 95%, 85% and 75%, 78% respectively for FC-ILC as well as Planck Commander, NILC, and SMICA maps calculated in an identical way. The 78% mask is the UT78 mask released by the Planck collaboration and is a union of masks used for different component separation methods.

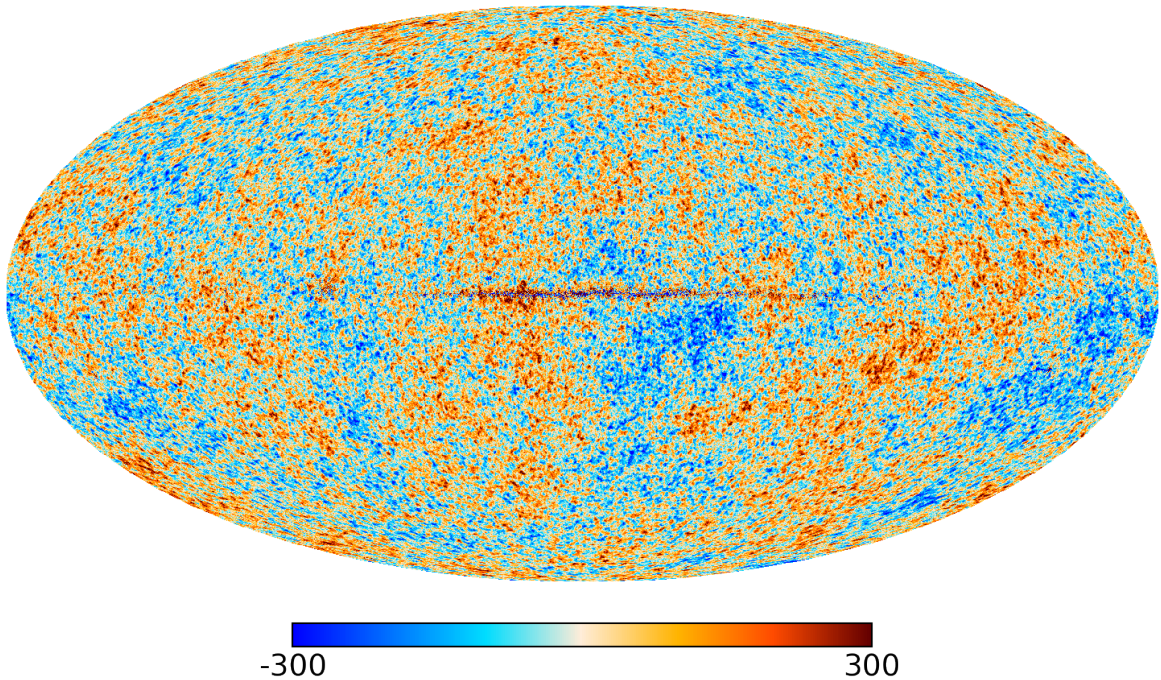


Figure 8: The Planck full mission FC-ILC map. The visibly contaminated region in the Galactic plane is included in the *bad partition*, the partition number 0 in Fig. 3, consisting 1% of the most contaminated pixels.

The solid line is the high ℓ power spectrum released by the Planck collaboration estimated from the 66%, 57% and 47% cleanest portion of the sky of 100 GHz, 143 GHz and 217 GHz maps respectively [1]. This power spectrum can therefore be taken as approximately the *true* C_ℓ s of our sky. Therefore, apart from the minor statistical fluctuations coming from having a large portion of the sky, the C_ℓ s estimated from the foreground cleaned maps should be close to these. In particular the deviation, both positive and negative, from the *true* power spectrum can be used as a measure of the foreground contamination in the CMB maps. The SMICA map shows significant negative bias at $\ell \geq 500$. The bias is much smaller in the NILC maps which lie between the Commander and SMICA solutions for most multipoles. The FC-ILC and Commander maps do not show this bias and are closer to the *clean* power spectrum released by Planck. The bias in SMICA maps decreases for 75% sky and also when using UT78 mask released by Planck as seen in Fig. 11. In particular there is a constant *negative* offset between SMICA and other maps at $\ell \gtrsim 500$.

4.3 Angular power spectrum at $800 \leq \ell \leq 2500$

We show the high ℓ angular power spectra, for $\ell \geq 800$ in Fig. 12 for 90% and 85% sky fraction and in Fig. 13 for 75% sky fraction and Planck UT78 mask. There is a large negative contamination in both SMICA and Commander maps for $\geq 85\%$ sky fractions around $\ell = 1100$. Even though, looking at $\ell > 1400$ it may seem that Commander and SMICA are cleaner than FC-ILC, this is in fact because there is a net negative bias at high ℓ . For the 85% power spectrum FC-ILC has similar excess at $\ell > 1400$ as Commander but FC-ILC does not have the negative contamination at $\ell < 1400$. There is in fact almost a constant offset between the SMICA and FC-ILC maps. For the UT78 mask, FC-

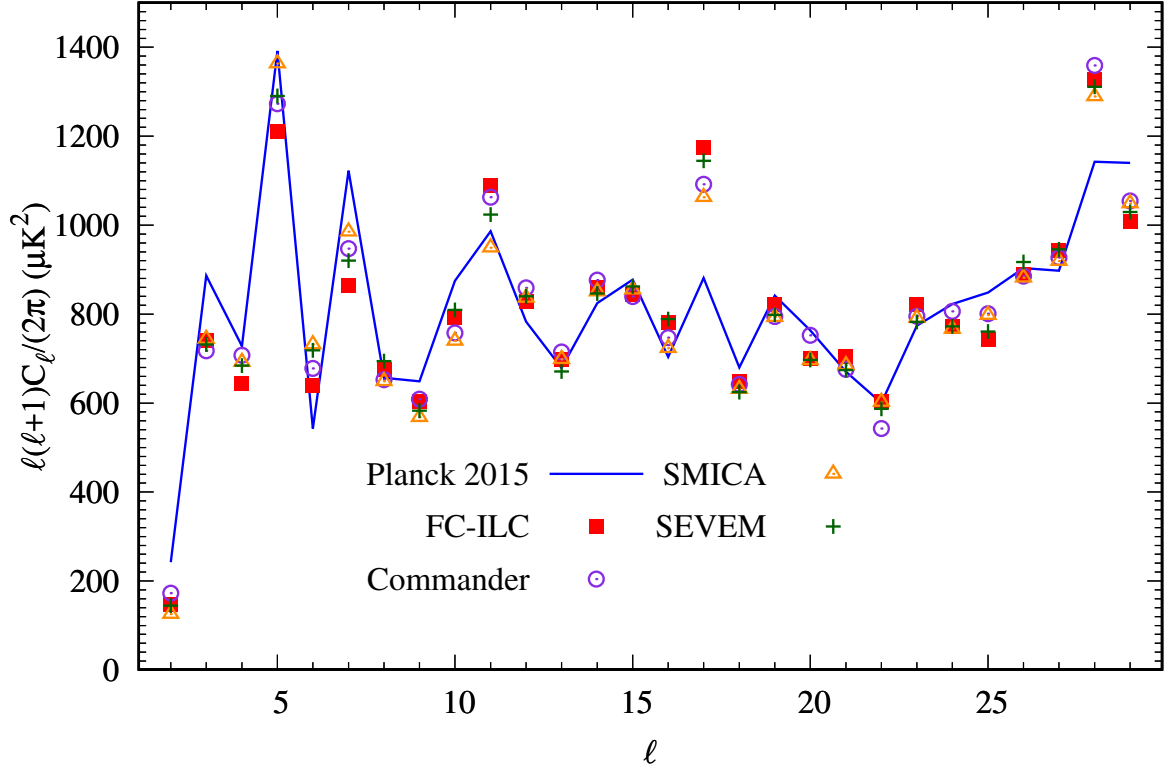


Figure 9: The low ℓ angular power spectrum of the CMB calculated on a sky fraction of 95% with a $30'$ apodized mask with the publicly available PolSpice software [30, 31]. The C_ℓ s have been corrected for the effect of the mask and the beam.

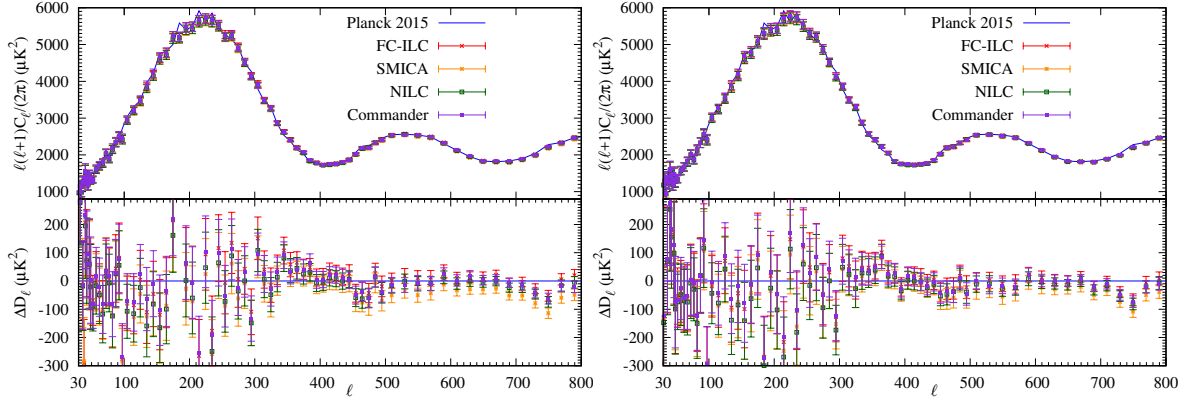


Figure 10: The mid- ℓ angular power spectrum of the CMB calculated on sky fractions of 95% (left panel) and 85% (right panel) with the masks apodized by a Gaussian with an apodization angle of $30'$. The bottom panels show the difference between the $D_\ell \equiv \ell(\ell + 1)C_\ell/(2\pi)$ calculated from the maps and the Planck PR2 release D_ℓ .

ILC power spectrum is almost identical to the SMICA and NILC power spectrum while Commander shows a larger excess. The NILC power spectrum lies between Commander and SMICA at most

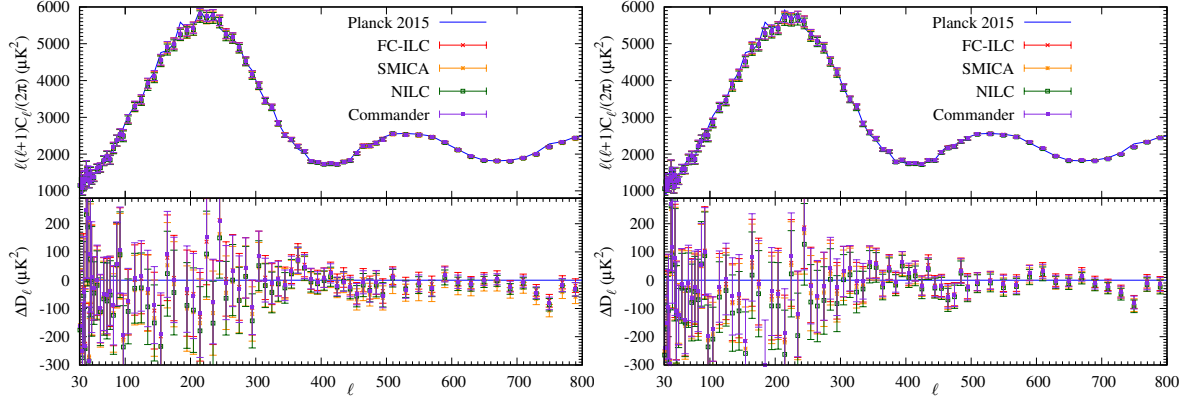


Figure 11: The mid- ℓ angular power spectrum of the CMB calculated on a sky fractions of 75% (left panel) and 78% (Planck UT78 mask, right panel). The bottom panels show the difference between the $D_\ell \equiv \ell(\ell + 1)C_\ell/(2\pi)$ calculated from the maps and the Planck PR2 release D_ℓ .

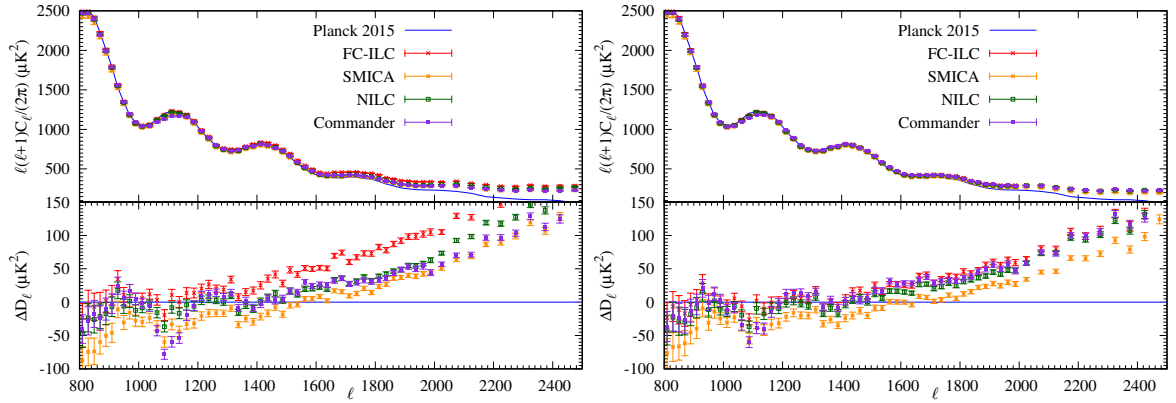


Figure 12: The high- ℓ angular power spectrum of the CMB calculated on a sky fractions of 90% (left panel) and 85% (right panel). The bottom panels show the difference between the $D_\ell \equiv \ell(\ell + 1)C_\ell/(2\pi)$ calculated from the maps and the Planck PR2 release D_ℓ .

multipoles and is closest to FC-ILC solution among the Planck public CMB maps.

5 Conclusions and remarks about possible improvements

We have presented a new approach to foreground cleaning and component separation in the multi-frequency CMB experiments. Our approach is to cluster together the data into groups or partitions, such that in each partition the foreground properties of the data are similar. This makes the problem of component separation more tractable since in each partition the data can be *accurately* described by a small number of components, ideally smaller than the number of frequency channels available. Our approach differs from the existing algorithms, which also try to cluster the data in pixel and/or harmonic space. Instead of a pre-determined clustering of data, we estimate the foreground properties from the data first summarizing it into a measure m and then use this measure m to partition the data *probabilistically*. This step of first estimating the foreground properties, other than the amplitude, is

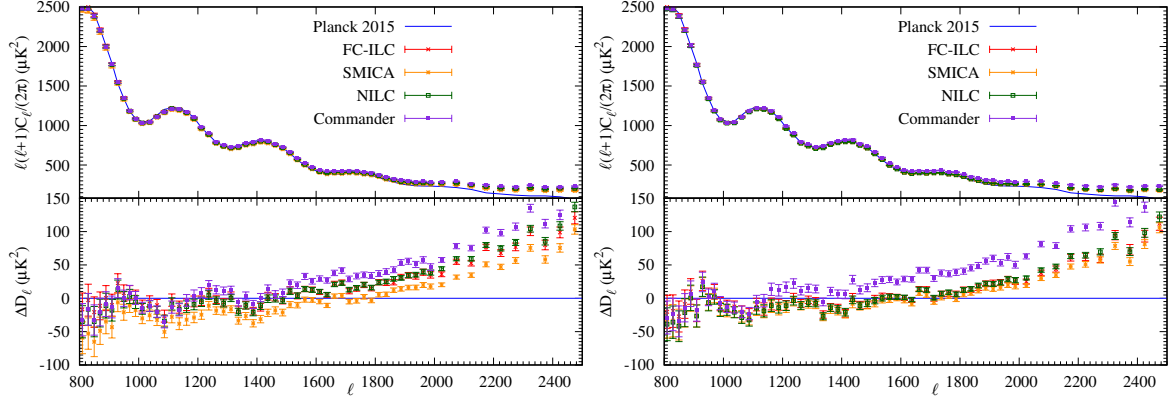


Figure 13: The high- ℓ angular power spectrum of the CMB calculated on a sky fractions of 75% (left panel) and 78% (Planck UT78 mask, right panel). The bottom panels show the difference between the $D_\ell \equiv \ell(\ell + 1)C_\ell/(2\pi)$ calculated from the maps and the Planck PR2 release D_ℓ .

the new ingredient. We have implemented our approach into an algorithm called FC-ILC. At present FC-ILC uses a single measure, constructed from two foreground dominated Planck HFI (high frequency instrument) channels and one clean channel, and performs the component separation in pixel space. However, the FC-ILC approach can be extended to use more than one measure and use harmonic space.

The second important new ingredient of our algorithm is to cluster the data randomly many times and use the average solution over these many random realizations of partitions. This probabilistic approach to the clustering of data allows the solution in a particular pixel to be influenced by all pixels close to it in terms of the measure m . There are no sharp boundaries in our solutions (CMB maps) that would need to be artificially smoothed.

The third ingredient is that we construct many different solutions, each with a different number of channels, and each solution at the best resolution allowed by the channels being used. These different resolution solutions are then combined in such a way so as to use the information from the best solutions available at a given scale ℓ .

We have tested our algorithm on FFP6 simulations and shown that it works as well as can be expected, especially compared with the results of other algorithms on the same simulations.

We have also applied our algorithm to the Planck PR2 temperature maps and produced new cleaned CMB maps (half-ring maps and full mission map) which are made publicly available for use by the cosmology community¹. We compare the properties of our maps with the Planck power spectrum results from the PR2 release as well as the foreground cleaned maps made available by the Planck collaboration. We find that while using the UT78 mask, giving approximately 78% of sky fraction for calculating the power spectrum, our results are consistent with SMICA, NILC and Commander maps, having similar residual contamination as SMICA, which is slightly better than Commander at high ℓ . However, when using a larger sky fraction, using our masks constructed by thresholding our measure m and the 545 GHz channel map, both Commander and SMICA show a *negative* contamination. In particular, there seems to be a constant offset between the SMICA and

¹<http://theory.tifr.res.in/~khatri/CMB>

FC-ILC power spectra, indicating that SMICA map has been *over-cleaned*. It is overall difficult to say which of the maps is best or most free of contamination. We hope that our independently produced maps with a different algorithm, with similar in amplitude if not smaller but qualitatively different residuals as the maps released by the Planck collaboration, would be useful in testing for the effect of residual foregrounds on cosmological parameters, in particular when studying the marginally significant anomalies.

We have chosen a particular clustering method based on a very simple one-dimensional measure of foreground shape. The shape of the foregrounds is of course much more complicated to be captured adequately by a single measure. We cannot therefore claim that our clustering is optimal. We have however shown that our simple foreground clustering approach is reasonable in the sense that it works as well as any of the other component separation algorithms used by the Planck collaboration. There is however definite room and clear direction for further improvement and optimization, especially using machine learning to cluster data using more than one measure, which we defer to a future publication.

Acknowledgements

I acknowledge interesting discussion with Ben Wandelt on CMB component separation methods. This work was supported by grant no. ECR/2015/000078 of Science and Engineering Research Board (SERB) of Department of Science and Technology (DST), Govt. of India. This work was also supported by MPG-DST partner group between Max Planck Institute for Astrophysics, Garching, Germany and Tata Institute of Fundamental Research, Mumbai, India funded by Max-Planck-Gesellschaft (MPG). This work made use of the HEALPix software [27] and its python version healpy.

References

- [1] Planck Collaboration, N. Aghanim, M. Arnaud, M. Ashdown, J. Aumont, C. Baccigalupi, A. J. Banday, R. B. Barreiro, J. G. Bartlett, N. Bartolo, and et al. Planck 2015 results. XI. CMB power spectra, likelihoods, and robustness of parameters. *A&A*, 594:A11, September 2016. [arXiv:1507.02704](#), [\[DOI\]](#), [\[ADS\]](#).
- [2] R. Keisler et al. A Measurement of the Damping Tail of the Cosmic Microwave Background Power Spectrum with the South Pole Telescope. *ApJ*, 743:28, 2011. [\[DOI\]](#), [\[ADS\]](#).
- [3] R. Hlozek et al. The Atacama Cosmology Telescope: A Measurement of the Primordial Power Spectrum. *ApJ*, 749:90, 2012. [\[DOI\]](#), [\[ADS\]](#).
- [4] P. A. R. Ade et al. Detection of B-Mode Polarization at Degree Angular Scales by BICEP2. *Physical Review Letters*, 112(24):241101, June 2014. [arXiv:1403.3985](#), [\[DOI\]](#), [\[ADS\]](#).
- [5] C. L. Bennett, D. Larson, J. L. Weiland, N. Jarosik, G. Hinshaw, N. Odegard, K. M. Smith, R. S. Hill, B. Gold, M. Halpern, E. Komatsu, M. R. Nolta, L. Page, D. N. Spergel, E. Wollack, J. Dunkley, A. Kogut, M. Limon, S. S. Meyer, G. S. Tucker, and E. L. Wright. Nine-year Wilkinson Microwave Anisotropy Probe (WMAP) Observations: Final Maps and Results. *ApJS*, 208:20, October 2013. [arXiv:1212.5225](#), [\[DOI\]](#), [\[ADS\]](#).
- [6] H. K. Eriksen, C. Dickinson, C. R. Lawrence, C. Baccigalupi, A. J. Banday, K. M. Górski, F. K. Hansen, P. B. Lilje, E. Pierpaoli, M. D. Seiffert, K. M. Smith, and K. Vanderlinde. Cosmic Microwave

Background Component Separation by Parameter Estimation. *ApJ*, 641:665–682, April 2006. [arXiv:astro-ph/0508268](#), [DOI], [ADS].

- [7] R. Khatri. Linearized iterative least-squares (LIL): a parameter-fitting algorithm for component separation in multifrequency cosmic microwave background experiments such as Planck. *MNRAS*, 451:3321–3339, August 2015. [arXiv:1410.7396](#), [DOI], [ADS].
- [8] R. Fernández-Cobos, P. Vielva, R. B. Barreiro, and E. Martínez-González. Multiresolution internal template cleaning: an application to the Wilkinson Microwave Anisotropy Probe 7-yr polarization data. *MNRAS*, 420:2162–2169, March 2012. [arXiv:1106.2016](#), [DOI], [ADS].
- [9] J. Delabrouille, J.-F. Cardoso, and G. Patanchon. Multidetector multicomponent spectral matching and applications for cosmic microwave background data analysis. *MNRAS*, 346:1089–1102, December 2003. [arXiv:astro-ph/0211504](#), [DOI], [ADS].
- [10] J.-F. Cardoso, M. Martin, J. Delabrouille, M. Betoule, and G. Patanchon. Component separation with flexible models. Application to the separation of astrophysical emissions. *ArXiv e-prints*, March 2008. [arXiv:0803.1814](#), [ADS].
- [11] D. Maino, A. Farusi, C. Baccigalupi, F. Perrotta, A. J. Banday, L. Bedini, C. Burigana, G. De Zotti, K. M. Górski, and E. Salerno. All-sky astrophysical component separation with Fast Independent Component Analysis (FASTICA). *MNRAS*, 334:53–68, July 2002. [arXiv:astro-ph/0108362](#), [DOI], [ADS].
- [12] J. Delabrouille, J.-F. Cardoso, M. Le Jeune, M. Betoule, G. Fay, and F. Guilloux. A full sky, low foreground, high resolution CMB map from WMAP. *A&A*, 493:835–857, January 2009. [arXiv:0807.0773](#), [DOI], [ADS].
- [13] K. K. Rogers, H. V. Peiris, B. Leistedt, J. D. McEwen, and A. Pontzen. SILC: a new Planck internal linear combination CMB temperature map using directional wavelets. *MNRAS*, 460:3014–3028, August 2016. [arXiv:1601.01322](#), [DOI], [ADS].
- [14] V. Sudevan, P. K. Aluri, S. K. Yadav, R. Saha, and T. Souradeep. Improved Diffuse Foreground Subtraction with the ILC Method: CMB Map and Angular Power Spectrum Using Planck and WMAP Observations. *ApJ*, 842:62, June 2017. [arXiv:1612.03401](#), [DOI], [ADS].
- [15] M. Tegmark and G. Efstathiou. A method for subtracting foregrounds from multifrequency CMB sky maps**. *MNRAS*, 281:1297–1314, August 1996. [arXiv:astro-ph/9507009](#), [DOI], [ADS].
- [16] M. Tegmark. Removing Real-World Foregrounds from Cosmic Microwave Background Maps. *ApJ*, 502:1–6, July 1998. [arXiv:astro-ph/9712038](#), [DOI], [ADS].
- [17] C. L. Bennett, R. S. Hill, G. Hinshaw, M. R. Nolta, N. Odegard, L. Page, D. N. Spergel, J. L. Weiland, E. L. Wright, M. Halpern, N. Jarosik, A. Kogut, M. Limon, S. S. Meyer, G. S. Tucker, and E. Wollack. First-Year Wilkinson Microwave Anisotropy Probe (WMAP) Observations: Foreground Emission. *ApJS*, 148:97–117, September 2003. [arXiv:astro-ph/0302208](#), [DOI], [ADS].
- [18] H. K. Eriksen, A. J. Banday, K. M. Górski, and P. B. Lilje. On Foreground Removal from the Wilkinson Microwave Anisotropy Probe Data by an Internal Linear Combination Method: Limitations and Implications. *ApJ*, 612:633–646, September 2004. [arXiv:astro-ph/0403098](#), [DOI], [ADS].
- [19] F. Vansyngel, B. D. Wandelt, J.-F. Cardoso, and K. Benabed. Semi-blind Bayesian inference of CMB map and power spectrum. *A&A*, 588:A113, April 2016. [arXiv:1409.0858](#), [DOI], [ADS].
- [20] M. Hazumi et al. LiteBIRD: a small satellite for the study of B-mode polarization and inflation from cosmic background radiation detection. In *Society of Photo-Optical Instrumentation Engineers (SPIE) Conference Series*, volume 8442, page 844219, September 2012. [DOI], [ADS].

- [21] A. Kogut, D. J. Fixsen, D. T. Chuss, J. Dotson, E. Dwek, M. Halpern, G. F. Hinshaw, S. M. Meyer, S. H. Moseley, M. D. Seiffert, D. N. Spergel, and E. J. Wollack. The Primordial Inflation Explorer (PIXIE): a nulling polarimeter for cosmic microwave background observations. *JCAP*, 7:25, 2011. [DOI], [ADS].
- [22] J. Delabrouille et al. Exploring cosmic origins with CORE: Survey requirements and mission design. *JCAP*, 4:014, April 2018. arXiv:1706.04516, [DOI], [ADS].
- [23] B. M. Sutin et al. PICO - the probe of inflation and cosmic origins. *Proceedings of the SPIE*, 10698:106984F, July 2018. arXiv:1808.01368, [DOI], [ADS].
- [24] Y. B. Zeldovich and R. A. Sunyaev. The Interaction of Matter and Radiation in a Hot-Model Universe. *ApSS*, 4:301–316, 1969. [DOI], [ADS].
- [25] Planck Collaboration, R. Adam, P. A. R. Ade, N. Aghanim, Y. Akrami, M. I. R. Alves, F. Argüeso, M. Arnaud, F. Arroja, M. Ashdown, and et al. Planck 2015 results. I. Overview of products and scientific results. *A&A*, 594:A1, September 2016. arXiv:1502.01582, [DOI], [ADS].
- [26] J. Delabrouille et al. The pre-launch Planck Sky Model: a model of sky emission at submillimetre to centimetre wavelengths. *A&A*, 553:A96, May 2013. arXiv:1207.3675, [DOI], [ADS].
- [27] K. M. Górski, E. Hivon, A. J. Banday, B. D. Wandelt, F. K. Hansen, M. Reinecke, and M. Bartelmann. HEALPix: A Framework for High-Resolution Discretization and Fast Analysis of Data Distributed on the Sphere. *ApJ*, 622:759–771, April 2005. arXiv:astro-ph/0409513, [DOI], [ADS].
- [28] J. Delabrouille and J. . Cardoso. Diffuse source separation in CMB observations. *ArXiv Astrophysics e-prints*, February 2007. arXiv:astro-ph/0702198, [ADS].
- [29] Planck Collaboration, P. A. R. Ade, N. Aghanim, C. Armitage-Caplan, M. Arnaud, M. Ashdown, F. Atrio-Barandela, J. Aumont, C. Baccigalupi, A. J. Banday, and et al. Planck 2013 results. XII. Diffuse component separation. *A&A*, 571:A12, November 2014. arXiv:1303.5072, [DOI], [ADS].
- [30] I. Szapudi, S. Prunet, and S. Colombi. Fast Analysis of Inhomogenous Megapixel Cosmic Microwave Background Maps. *ApJL*, 561:L11–L14, November 2001. [DOI], [ADS].
- [31] G. Chon, A. Challinor, S. Prunet, E. Hivon, and I. Szapudi. Fast estimation of polarization power spectra using correlation functions. *MNRAS*, 350:914–926, May 2004. arXiv:astro-ph/0303414, [DOI], [ADS].
- [32] E. Hivon, K. M. Górski, C. B. Netterfield, B. P. Crill, S. Prunet, and F. Hansen. MASTER of the Cosmic Microwave Background Anisotropy Power Spectrum: A Fast Method for Statistical Analysis of Large and Complex Cosmic Microwave Background Data Sets. *ApJ*, 567:2–17, March 2002. arXiv:astro-ph/0105302, [DOI], [ADS].
- [33] M. Tristram, J. F. Macías-Pérez, C. Renault, and D. Santos. XSPECT, estimation of the angular power spectrum by computing cross-power spectra with analytical error bars. *MNRAS*, 358:833–842, April 2005. arXiv:astro-ph/0405575, [DOI], [ADS].
- [34] Planck Collaboration, R. Adam, P. A. R. Ade, N. Aghanim, M. Arnaud, M. Ashdown, J. Aumont, C. Baccigalupi, A. J. Banday, R. B. Barreiro, and et al. Planck 2015 results. IX. Diffuse component separation: CMB maps. *A&A*, 594:A9, September 2016. arXiv:1502.05956, [DOI], [ADS].

A Convergence of FC-ILC solution

There are two important parameters to be chosen in the FC-ILC algorithm: The number of random realization of partitions to be done and the number of partitions to be chosen. The number of random realizations is a simpler choice to make, more number of realizations would result in smoother

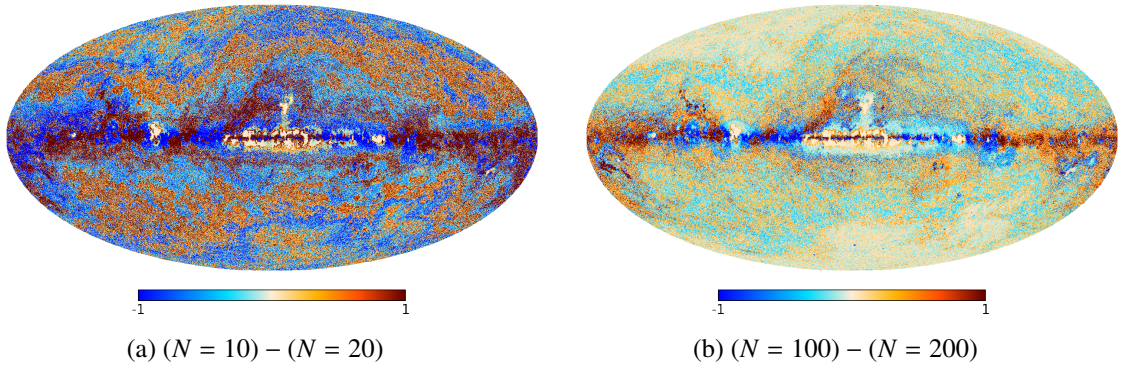


Figure 14: The change in FC-ILC solution when doubling the number of random realization of partitions from $N = 10$ to $N = 20$ (left panel) and from $N = 100$ to $N = 200$ (right panel). The results are shown for the FFP6 simulation. Similar results are obtained also for the real sky data. The difference map has been degraded from the original $N_{\text{side}} = 2048$ to $N_{\text{side}} = 512$ for this figure. The color scale ranges from $-1 \mu\text{K}$ to $1 \mu\text{K}$. Note that most of the Galactic plane also undergoes $< 1 \mu\text{K}$ change when going from 100 to 200 random realizations.

boundaries. Once the solution is converged, additional realizations would not change the solution. We show in Fig. 14 the change in FC-ILC solution when doubling the number of random realizations from $N = 10$ to $N = 20$ and also the change in the solution when doubling the number of realizations from $N = 100$ to $N = 200$ for the FFP6 simulation. We see that after 100 realizations, the change in the solution in any pixel at HEALPix $N_{\text{side}} = 512$ is $\ll 1 \mu\text{K}$ over most of the sky. We therefore fix the number of realizations to 100. The size of a pixel at $N_{\text{side}} = 512$ is 6.87 arcmin, close to the 5 arcmin resolution of the CMB map and is therefore a good resolution choice to test the convergence of the algorithm.

We show the effect of changing the number of pixel clusters (including two fixed clusters covering the dirtiest portions of the sky) in Fig. 15. We show the difference in FC-ILC solution for different choices of number of clusters from the solution for 13 clusters. The difference in solution is less than $1 \mu\text{K}$ if we change the number of pixel clusters to 11 or 15 but we see a slightly larger difference if we choose the number of clusters to be too small (5) or too large (23). Choosing the number of clusters around 13 gives the best results as gauged by comparison of the input and output power spectra and we choose to partition the map into 13 clusters (including 2 contaminated or bad clusters with extreme values of the foreground measure m).

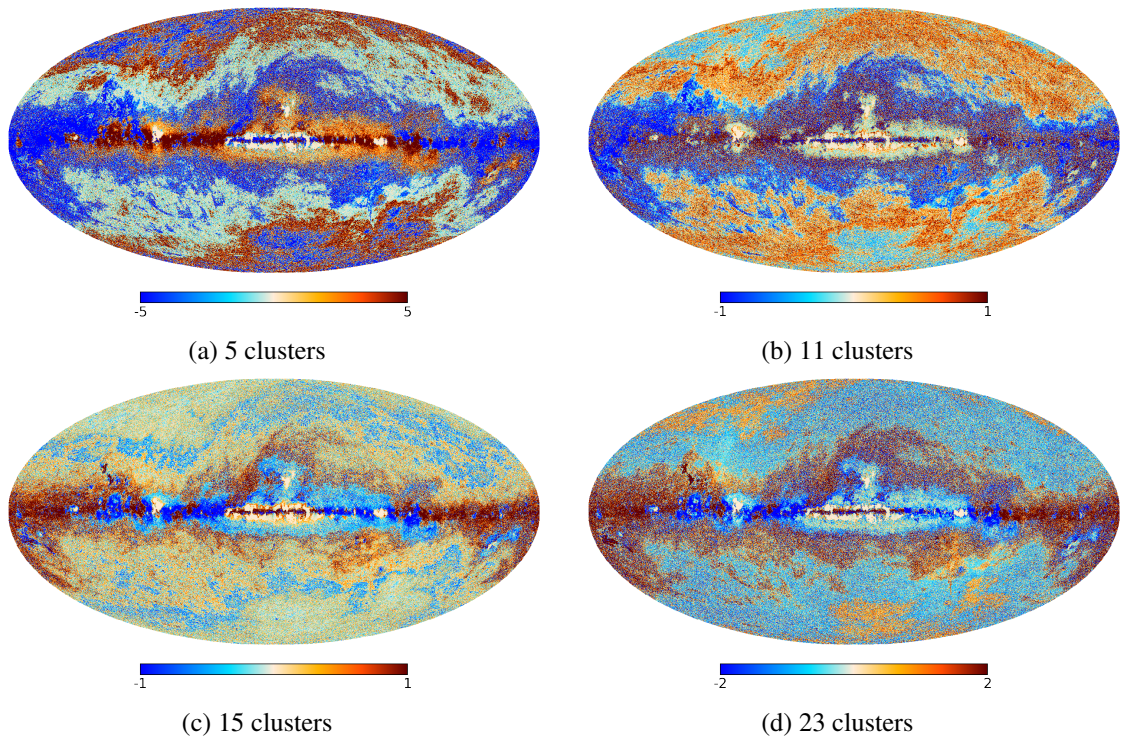


Figure 15: The change in FC-ILC solution when changing the number of clusters the map is divided into. All maps are difference from the solution obtained with 13 clusters. The results are shown for the FFP6 simulation. Similar results are obtained also for the real sky data. The difference map has been degraded from the original $N_{\text{side}} = 2048$ to $N_{\text{side}} = 512$ for this figure. The color scale ranges from $-1 \mu\text{K}$ to $1 \mu\text{K}$ for the difference maps for 11 and 15 clusters and larger ranges for the other two difference maps.